Biosensors and Bioelectronics 241 (2023) 115700

Contents lists available at ScienceDirect

Biosensors and Bioelectronics

journal homepage: www.elsevier.com/locate/bios

# Rapid and simultaneous multiple detection of a tripledemic using a dual-gate oxide semiconductor thin-film transistor-based immunosensor

Sehun Jeong [a,1], Seong Uk Son [b,c,1], Jingyu Kim [a], Seong-In Cho [a], Taejoon Kang [b,d], Sunjoo Kim [e,f,g], Eun-Kyung Lim [b,c,d,**], Sang-Hee Ko Park [a,*]

[a] Department of Materials Science and Engineering, Korea Advanced Institute of Science and Technology, 291 Daehak-ro, Yuseong-gu, Daejeon, 34141, Republic of Korea
[b] BioNanotechnology Research Center, Korea Research Institute of Bioscience and Biotechnology, 125 Gwahak-ro, Yuseong-gu, Daejeon, 34141, Republic of Korea
[c] Department of Nanobiotechnology, Korea Research Institute of Bioscience and Biotechnology, School of Biotechnology, University of Science and Technology (UST), 217 Gajeong-ro, Yuseong-gu, Daejeon, 34113, Republic of Korea
[d] School of Pharmacy, Sungkyunkwan University, Suwon, 16419, Republic of Korea
[e] Department of Laboratory Medicine, Gyeongsang National University Changwon Hospital, Changwon, 51472, Republic of Korea
[f] Gyeongnam Center for Infectious Disease Control and Prevention, Changwon, 51154, Republic of Korea
[g] Gyeongsang National University College of Medicine, Gyeongsang Institute of Health Sciences, Jinju, 52727, Republic of Korea

ARTICLE INFO

*Keywords:*
Multiple detection
Dual-gate thin-film transistor
Tripledemic
Point-of-care test

ABSTRACT

The simultaneous infection with a tripledemic—simultaneous infection with influenza A pH1N1 virus (Flu), severe acute respiratory syndrome coronavirus 2 (SARS-CoV-2), and respiratory syncytial virus (RSV)—necessitates the development of accurate and fast multiplex diagnostic tests. The coronavirus disease 2019 (COVID-19) pandemic has emphasized the importance of virus detection. Field-effect transistor (FET)-based immunobiosensors have a short detection time and do not require labeling or polymerase chain reaction. This study demonstrates the rapid, sensitive detection of influenza A pH1N1, SARS-CoV-2, and RSV using a multiplex immunosensor based on a dual-gate oxide semiconductor thin-film transistor (TFT), a type of FET. The dual-gate oxide TFT was modified by adjusting both top and bottom gate insulators to improve capacitive coupling to approximately 120-fold amplification, exhibiting a high pH sensitivity of about 10 V/pH. The dual-gate oxide TFT-based immunosensor detected the target proteins (hemagglutinin (HA) protein of Flu, spike 1 (S1) protein of SARS-CoV-2, and fusion protein of RSV) of each virus, with a limit of detection of approximately 1 fg/mL. Cultured viruses in phosphate-buffered saline or artificial saliva and clinical nasopharynx samples were detected in 1-μL sample volumes within 60 s. This promising diagnosis could be potentially as point-of-care tests to facilitate a prompt response to future pandemics with high sensitivity and multiplexed detection without pretreatment.

## 1. Introduction

The increasing frequency of infectious diseases worldwide threatens human health and lives (Baker et al., 2022). Due to the recent global pandemic of coronavirus disease 2019 (COVID-19), as of 1:56pm CEST, August 2nd, 2023, more than 768 million confirmed cases and more than 6.9 million deaths worldwide reported to WHO. In addition, the increased possibility of another pandemic (Kang et al., 2023; Merced-Morales et al., 2022) necessitate the development of biosensors enabling rapid diagnosis and classification of infectious diseases to prevent complex twin- and tripledemics involving multiple pathogens (Kim et al., 2021; Zheng et al., 2023). The Centers for Disease Control (CDC) issued a warning of the widespread simultaneous occurrence of three prominent respiratory viruses—influenza A virus, severe acute respiratory syndrome *coronavirus 2 (*SARS-CoV-2), and respiratory syncytial virus (RSV)—causing severe respiratory illness (Kekatos, 2022). The symptoms of these infections (including fever and sore throat) are similar; an incorrect diagnosis poses a serious health threat; therefore, it

* Corresponding author.
** Corresponding author. BioNanotechnology Research Center, Korea Research Institute of Bioscience and Biotechnology, 125 Gwahak-ro, Yuseong-gu, Daejeon, 34141, Republic of Korea.
*E-mail addresses:* eklim1112@kribb.re.kr (E.-K. Lim), shkp@kaist.ac.kr (S.-H. Ko Park).
[1] These authors contributed equally to this work.

https://doi.org/10.1016/j.bios.2023.115700
Received 26 June 2023; Received in revised form 22 August 2023; Accepted 19 September 2023
Available online 20 September 2023

is necessary to prescribe appropriate treatment based on accurate and prompt diagnosis (Li et al., 2020). Molecular diagnostic techniques, such as real-time polymerase chain reaction (PCR) and quantitative PCR (qPCR), are standard diagnostic methods for these diseases (Kang et al., 2022; T. Y. Kim et al., 2022; Moon et al., 2020; Ravina Dalal et al., 2020; Ruest et al., 2003; Todd et al., 2021). Although these methods are associated with high accuracy and low errors, they are relatively expensive and complicated requiring specialized operation skills. Immunodiagnostic systems offer the advantage of rapid detection because they do not require complex preprocessing of samples such as DNA and RNA extraction and purification required in molecular diagnosis. (G. G. Chen et al., 2022; Shukla et al., 2022; Son et al., 2023, 2019); however, they have lower sensitivity and limited specificity than molecular diagnostics.

Field-effect transistor (FET)-based immuno-biosensors, biosensors that detected targets via antibody-antigen reaction, were composed of sensing membrane and transducer (Martins et al., 2021). Electrode or active channel layer was modified as sensing membrane with linker and antibody to bind specific target proteins or viruses (Hwang et al., 2020; Poghossian et al., 2020; B. Wang et al., 2022; Zhao et al., 2021). The antibody-antibody reaction on sensing membrane was transduced to electrochemical signal and transmitted as output signal by FET as transducer (Deng et al., 2022; Masurkar et al., 2020). FET-based immuno-biosensors have been widely researched owing to their high sensitivity, selectivity, potential multiplex detection ability, short response time, real-time monitoring ability, simple point-of-care testing, and low power consumption (Lee et al., 2021; Park et al., 2012; Sadighbayan et al., 2020; Y. Wang et al., 2022). From these advantages, advanced immunnosensors based on FET for various targets were developed such as stress biomarker cortisol, Interleukin-6 biomarker, and Alzheimer's disease (Chandra Barman et al., 2021; Kwon et al., 2021; Tlili et al., 2011). Recently, FET structures have been improved by incorporating novel materials, such as graphene, carbon nanotubes, and oxide semiconductors (Afroj et al., 2021; Baldacchini et al., 2020; J. J. Chen et al., 2022; Fathi-Hafshejani et al., 2021; Kajale et al., 2021; Manigrasso et al., 2022; Park et al., 2022; Piccinini et al., 2022; Shahdeo et al., 2022; Yahya et al., 2022; Zamzami et al., 2022; Zhang et al., 2022). Novel materials, such as carbon nanomaterials and semiconductor, are suitable for sensor applications due to adjustable electrical properties and great electrochemical properties (Liu et al., 2021). Especially,

Oxide semiconductors show excellent swing characteristics with rapidly switching between on/off (Kamiya et al., 2010). An oxide semiconductor-based FET operating in this advanced subthreshold regime is suitable for sensitive sensor with super-low leakage current, high stability, high mobility, and superior scalability (Baldacchini et al., 2020; Jang et al., 2021; Ji et al., 2020; Ko et al., 2019; Park et al., 2017), allowing for a wide detection concentration range and low limits of detection (LODs) (Kim et al., 2021; Ranjan et al., 2021; Seo et al., 2020; Tang et al., 2020).

In this study, we developed a multiplexed sensor device based on oxide semiconductor thin-film transistors (TFTs), a specific type of FET fabricated as thin-film layers, designed as an optimized dual-gate structure. The signal from sensing membrane was amplified and transmitted as much as capacitive coupling, the ratio of voltages transferred between two electrodes through coupled capacitances (Ahn et al., 2020). Herein, we present a multiplexed sensor device based on dual-gate oxide semiconductor TFTs designed as an optimized dual-gate structure to amplify biosensing via the capacitive coupling. Herein, we present a multiple immune-diagnostic sensor that could rapidly detect and discriminate influenza A virus, SARS-CoV-2, and RSV.

## 2. Materials and methods

### 2.1. Fabrication of dual-gate oxide semiconductor TFTs

Dual-gate oxide semiconductor TFTs were fabricated, as shown in Fig. S1a. The substrate, 150 nm-thick indium tin oxide (ITO)-coated glass (Geomatec Co., Ltd., Yokohama, Japan), was patterned for the bottom gate, the sensing membrane. The $Al_2O_3$ dielectric layer was deposited at 300 °C by plasma-enhanced atomic layer deposition (PEALD) for bottom gate insulators with a split-thickness (5, 10, 20, and 40 nm). The Al-doped ITZO (Al:ITZO) layer was subsequently grown by radio frequency (RF) sputtering at room temperature under 40% oxygen partial pressure. The Al:ITZO layer was patterned for the oxide semiconductor active channel with 40 μm width and 20 μm length and pre-annealed at 350 °C under an oxygen atmosphere for 2 h. A 150 nm-thick molybdenum (Mo) layer was deposited by direct current (DC) sputtering and patterned for source and drain (S/D) electrodes. The $SiO_2$ dielectric layer was deposited at 300 °C via plasma-enhanced chemical vapor deposition (PECVD), followed by 30 nm-thick SiO2 PEALD deposition with a resultant total split-thickness of 200, 400, and 600 nm. After contact hole patterning, a 150 nm-thick Mo layer was DC sputtered and patterned for the top gate electrode. All patterning was processed using photolithography with wet etching. Finally, vacuum annealing was performed.

### 2.2. Analysis of electrical characteristics

The electrical properties of the dual-gate oxide semiconductor TFTs were evaluated using a semiconductor parameter analyzer HP4156A (HP Inc., Palo Alto, California, USA) and probe station. For transfer curve measurements, the bottom gate and drain-source voltage were 0 V and 0.1 V, respectively, when the top gate voltage was swept. To confirm the hysteresis of the TFTs, the top gate voltage was swept in both forward and backward directions. CCRs were confirmed by transfer curve shift when constant bias was applied to the bottom gate (number of experiments: 10).

The transfer curve shift was measured by reference voltage ($V_R$), which was the value of $V_{tg}$ with drain-source current ($I_{ds}$) of $10^{-10}$ A on the transfer curve. pH sensitivities were confirmed using buffer solution (Daejung Chemicals & Metals Co., Ltd., Gyeonggi-do, Korea) with specific pH 3, 7, 9, and 11 (number of experiments: 10). For real-time detection, drain-source voltage and both gate voltages were fixed at 0.1 V and 0 V, respectively. The normalized current was calculated from real-time drain-source current and initial drain-source current ($I_0$) of the virus and canceling sensors according to Equation (1).

$$\left[Normalized\ current = \frac{I_{main} - I_{main,0}}{I_{main,0}} - \frac{I_{canceling} - I_{canceling,0}}{I_{canceling,0}}\right] \quad (1)$$

To reduce the possibility of false positives and enable precise target detection, the normalized response was calculated by subtracting the change rate the canceling sensor's $I_{ds}$ from the change in $I_{ds}$ the main sensor 60 s after sample injection. For contact between the probe tip and the solution on the sensing membrane, an Ag/AgCl electrode LF-1-100 (Innovative Instruments Inc., Tampa, Florida, USA) was used as a reference electrode.

### 2.3. Immobilization of antibodies

Antibodies were attached to the ITO-coated bottom gate of the FET-based immune-biosensor using 3-Aminopropyltriethoxysilane (APTES) and 1-Ethyl-3-(3-dimethylaminopropyl)carbodiimide/N-Hydroxysuccinimide (EDC/NHS) coupling reactions (Fig. S1b). Anti-Influenza A Virus Hemagglutinin (HA) antibody (ab119966, Abcam, Cambridge, UK), anti-Respiratory Syncytial Virus (anti-RSV) fusion protein antibody (ab24011, Abcam, Cambridge, UK), and anti-SARS-CoV-2 S1 protein

antibody (CABT-CS-141, Creative Diagnostics®, Shirley, New York, USA) were employed to specifically bind to proteins of the respective viruses. First, the ITO-coated sensing region was washed with acetone and ethanol. The surface was then modified using $O_2$ plasma and treated with 10% APTES in ethanol at 80 °C for 1 h to expose $NH_2$ functional groups on the surface. The surface was washed with acetone and DW three times and analyzed using X-ray photoelectron spectroscopy (XPS); K-Alpha (Thermo Scientific Inc., Waltham, Massachusetts, USA). The sensing area was then treated with 25 mM EDC and 50 mM NHS in a 1:1 ratio and reacted with 1 mg/mL antibody at room temperature for 4 h. Remaining EDC/NHS was washed three times with DW, and the sensing area was blocked with 1% bovine serum albumin (BSA) at room temperature for 30 min. The prepared immunosensor was confirmed to have attached antibodies using an atomic force microscopy (AFM) nanoscope (Bruker Co., Billerica, Massachusetts, USA) and direct ELISA.

### 2.4. Viruses

Influenza A virus (National Culture Collection for Pathogens [NCCP] No. 42013), SARS-CoV-2 (NCCP 43331), and RSV (NCCP No. 40104) were provided by the NCCP, which the Korea National Institute of Health operates. All experiments involving the viruses were performed at the Korea Centers for Disease Control and Prevention (KCDC)-approved biosafety level (BL-2 and BL-3) facility of the Korea Research Institute of Bioscience and Biotechnology (KRIBB) in accordance with institutional biosafety requirements.

### 2.5. Real-time detection

Real-time target protein detection of influenza A HA protein (ab256439, Abcam, Cambridge, UK), SARS-CoV-2 S1 protein (DAGC210, Creative Diagnostics®, Shirley, New York, USA), and RSV fusion protein (40037-V08B, SinoBiological, Beijing, China) was performed (number of experiments: 5). To verify selectivity, 1 μL high (1 pg/mL) concentration protein solutions in 0.01 × PBS were dropped on the sensing membrane. To verify sensitivity, 1 μL of increasing concentrations ($10^{-1}$, $10^{\circ}$, $10^{1}$, and $10^{2}$ fg/mL) of protein solution in 0.01 × PBS was dropped on the sensing membrane. Cultured influenza A pH1N1 (NCCP No. 42013), SARS-CoV-2 (NCCP No. 43331), and RSV (NCCP No. 40104) were used to confirm virus detection, selectivity, and sensitivity were confirmed using a high concentration ($10^{3}$ $TCID_{50}$/mL) and a concentration range ($10^{-1}$, $10^{\circ}$, $10^{1}$, and $10^{2}$ $TCID_{50}$/mL), respectively (number of experiments: 5). A concentration range ($10^{-1}$, $10^{\circ}$, $10^{1}$ and $10^{2}$ $TCID_{50}$/mL) of a mixture of cultured influenza A pH1N1, SARS-CoV-2, and RSV was prepared in an artificial saliva mixture containing 0.01 × PBS and artificial saliva (1700-0324, Pickering Laboratories Inc., Mountain View, California, USA) at a 9:1 ratio. For clinical sample testing, patient samples were injected 60 s after the injection of control (negative) samples. Sensitivity was measured using the normalized response value 60 s after sample injection.

### 2.6. Acquisition of clinical nasopharynx samples

A total of 58 samples were acquired from Gyeongsang National University College of Medicine, including 9 influenza A-infected patient samples, 9 influenza B-infected patient samples, 20 COVID-19-infected patient samples, 10 RSV-infected patient samples and 10 non-patient (uninfected) models. Samples collected by swab from the patient's nasopharynx were included in viral transport medium (VTM) and were not subjected to any pretreatment such as concentration or dilution. These samples were provided with the quantitative reverse transcription polymerase chain reaction (qRT-PCR) data. The protocol for this study was reviewed and approved by the Institutional Review Board (IRB) of Gyeongsang National University College of Medicine in Jinju, Republic of Korea (IRB approval number: 2022-10-012).

## 3. Results and discussion

### 3.1. Characteristics of the dual-gate TFT-based multiplexed Immunosensor

Scheme 1 illustrated the entire processes of detecting three viruses (SARS-CoV-2, RSV, and Influenza A pH1N1) using a dual-gate oxide semiconductor thin-film transistor-based immune-biosensor. A clinical sample collected with a nasopharyngeal swab from a patient was injected onto the sensing membrane in one drop. Main sensors selectively detected each target elements in the sample. Canceling sensor measured noise caused by non-target elements. Through these, triple-demic viruses were simultaneously detected in real-time.

TFT devices were fabricated with a dual-gate structure following the procedures illustrated in Fig. S1a. In the dual-gate TFT structure, the active channel layer was wrapped from top and bottom in a gate insulator (GI), called top and bottom GI, respectively. In this dual-gate oxide TFT-based immunosensors, bottom gate was extended and acted as a sensing membrane. The signal due to the surface potential change of the sensing membrane caused the change of bottom gate voltage. The bottom gate voltage change was amplified and transmitted to the top gate by capacitive coupling ratio (CCR), which means the ratio at which the voltage applied to one gate electrode is transferred to the other gate electrode (Baek et al., 2023). Through this capacitive coupling phenomenon, TFT devices amplified the electrical signal without additional amplification devices. The signal amplification factor, CCR, increases with an increased capacitance ratio (Ahn et al., 2020). The top and bottom GI capacitance ratio could be controlled by adjusting the material and thickness. Top gate insulators were deposited by PECVD after depositing thin layer by PEALD to improve the interface characteristics by reducing the damage to the active channel oxide semiconductor (Barron, 1996; Dingemans et al., 2012; Ovanesyan et al., 2019). The material of $SiO_2$ was applied as top GI due to stable and suitability for both deposition processes (Cho et al., 2022; Jung et al., 2016). The material of $Al_2O_3$ with a higher dielectric constant compared to SiO2 was applied as bottom GI due to excellent insulating layer performance such as low leakage for oxide semiconductor-based TFTs (Chen et al., 2013; Kim et al., 2009; Ma et al., 2018). The top and bottom GI materials were fixed to $SiO_2$ and $Al_2O_3$, respectively.

The performance of the TFT devices with adjusting top and bottom GI thickness was confirmed by sensing electrical potential and pH as shown on Table 1. To quantify the performance of the TFT devices as electrical potential sensors, transfer shift characteristics were measured with constant voltage bias on the bottom gate, which serves as the sensing membrane (Figs. S2b and e). The degree of transfer curve shift was measured as the change in reference voltage ($V_R$), which was top gate bias ($V_{tg}$) with a drain-source current ($I_{ds}$) of $10^{-10}$ A on transfer I-V characteristics. The value of CCR was measured as the degree to which the VR changed per unit constant bias applied. TFT devices with 5 nm-thick top GI and 600 nm-thick bottom GI exhibited a CCR of 120.17 ± 3.17 V/V. This value indicated that voltage of external electrical signals entering the sensing membrane were amplified approximately 120-fold. The performance of the TFT devices as a pH sensor was measured as the changes in $V_R$ on the I-V curve brought about by buffer solutions of varied pH values to confirm the ability to detect the surface potential change (Figs. S2c and f) (Das et al., 2014; Lee et al., 2021). TFT devices with 5 nm-thick bottom GI and 600 nm-thick top GI exhibited 10.64 ± 0.67 V/pH, considerably larger than the Nernst limit of 0.060 V/pH (Knopfmacher et al., 2010). All linear fittings exhibited $R^2$ values > 0.99, confirming the TFT device as an effective electrical potential and pH sensor.

TFT devices with bottom GI thickness less than 5 nm showed no subthreshold regime where TFT-based immuno-biosensors were operated and showed conductive characteristics. In the dual-gate oxide TFTs with 5 nm-thick bottom GI, the degree of signal amplification was increased as the top GI thickness was increased; however, signals were

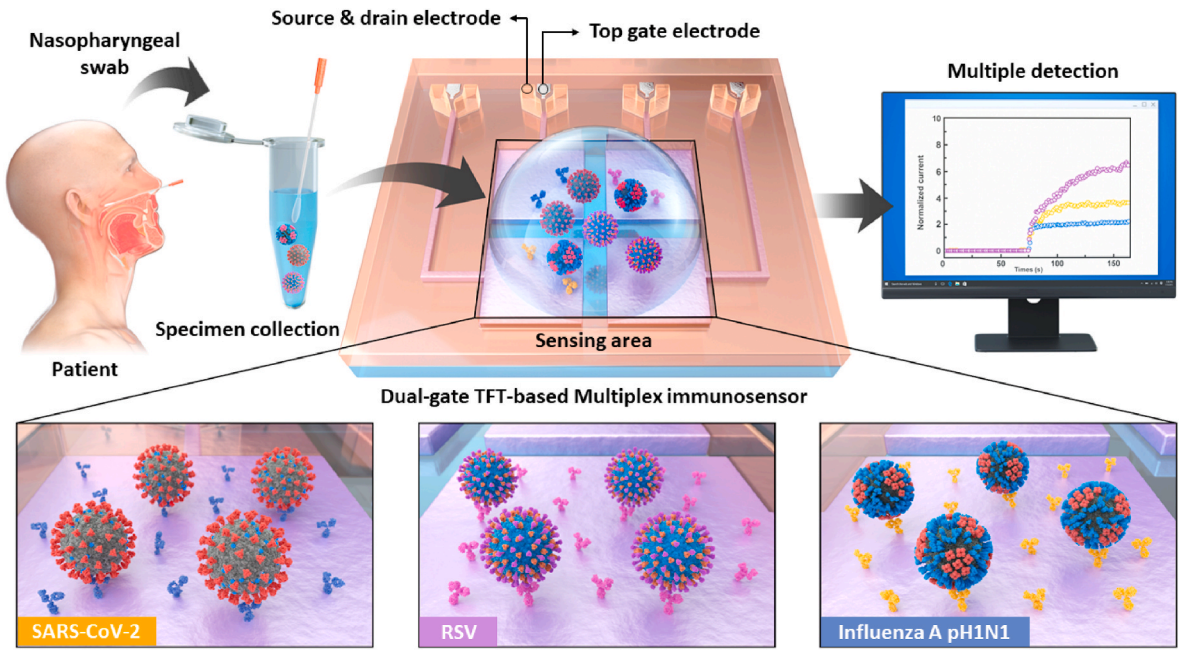


**Scheme 1.** Representation of multiple detections of tripledemic viruses using a dual-gate oxide semiconductor thin-film transistor.

**Table 1**
Improvement in sensor performance via gate insulator (GI) modification with confirmation of capacitive coupling ratio (CCR) and pH sensitivity.

| | Bottom gate insulator | | | | Top gate insulator | | | |
|---|---|---|---|---|---|---|---|---|
| GI Thickness | 40 nm | 20 nm | 10 nm | 5 nm | 200 nm | 400 nm | 600 nm | 800 nm |
| CCR (V/V) | 8.108 ± 0.05 | 14.45 ± 0.08 | 25.88 ± 0.27 | 40.28 ± 1.01 | 40.28 ± 1.01 | 76.21 ± 1.73 | 120.17 ± 3.17 | 148.50 ± 1.70 |
| Sensitivity (V/pH) | 0.631 ± 0.01 | 1.129 ± 0.02 | 1.931 ± 0.05 | 3.058 ± 0.17 | 3.058 ± 0.17 | 5.683 ± 0.23 | 10.64 ± 0.67 | 11.45 ± 0.47 |

over the measurable range of the measuring instruments when top GI thickness exceeded 600 nm. Thus, TFT devices were structured with 5 nm-thick bottom GI and 600 nm-thick top GI.

A schematic representation of the dual-gate TFT-based immune-biosensor is shown in Fig. 1a. Optical and transmission electron microscopy (TEM; JEM-2100F electron microscope) (JEOL Ltd., Tokyo, Japan) were used to investigate the top-view and cross-sectional structure of the fabricated immunosensor. Fig. 1b and c shows top-view optical microscopy images, and Fig. 1d shows a cross-sectional image from TEM (JEOL Ltd.). Fig. 1e shows the transfer characteristics of the immunosensor based on the optimized TFT device by $V_{tg}$ sweeping with grounded bottom gate bias ($V_{bg}$). The immunosensor exhibited a $V_{tg}$ of 0 V within the subthreshold regime, where $I_{ds}$ was exponentially changed as a function of gate voltage between the on and off states (Gao et al., 2010). To minimize power consumption, the immunosensor was operated at low $I_{ds}$ and zero voltage-fixed Vtg for the subthreshold regime. Surface potential changes in the sensing membrane induced by target binding were amplified by a factor of the CCR, resulting in large current changes. As seen in Figs. S2a and d, the transfer I-V characteristics exhibited a more gradual slope for the subthreshold regime, increasing the top and bottom GI capacitance ratio. The subthreshold regime, therefore, allows for a wider operating range with improved signal sensitivity (Ahn et al., 2020; Baek and Kanicki, 2012). In addition to improvement by operating in the subthreshold regime (Baek et al., 2023), outstanding sensitivity was shown with signal amplification obtained by adjusting GI of the dual-gate oxide TFT. Immunosensors with a high CCR exhibit a large signal amplification factor. Hysteresis, the difference between the forward and backward sweeps of the transfer curves caused by various defects (Choi et al., 2020; Ye et al., 2017), can cause leakage and $I_{ds}$ changes without external signals when immunosensors are used in real-time. This study reduced hysteresis by eliminating defects in the interface between the GI and active channel layer through thermal annealing (Fuh et al., 2014; Ko et al., 2019). The inset in Fig. 1e shows negligible hysteresis, confirming that the multiplexed immunosensor is suitable for ultra-sensitive real-time target detection with precise $I_{ds}$ responses and low power consumption.

Performance of TFT devices with adjusting both top and bottom GI was confirmed as electrochemical sensor by sensing surface potential from constant bias and pH buffer solution. The dual-gate oxide TFTs showed outstanding sensitivities via subthreshold operation and capacitive coupling. These TFT showed excellent electrical characteristics such as negligible hysteresis. The multiplexed detection of three viruses was designed using the immunosensor based on these dual-gate oxide TFTs.

### 3.2. Antibody immobilization on the dual-gate TFT-based sensor

An immunosensing area was applied to the ITO-coated bottom gate via APTES coating and antibody attachment. First, the silane of APTES forms a covalent bond with the silanol of ITO glass, and is coated on the surface. Subsequently, the ITO glass surface with the exposed amine group forms a peptide bond with the antibody's carboxyl group (COO-) through an EDC/NHS coupling reaction (Figs. S3a and e). Antibodies bound to the ITO glass in this way made the immunosensing area of the bottom gate.

Coating of the glass with APTES was confirmed using XPS analysis. XPS measures the energy of photoelectrons emitted when incident X-rays on the surface of a sample. This allows for the determination of composition and chemical bonding state of the sample's surface. While the 'N' element peak was absent in the bare ITO glass, the APTES coated ITO glass showed a distinct N 1s peak at 398.4 eV (Fig. S3b), attributable to the presence of APTES's amine group. These results indicate the

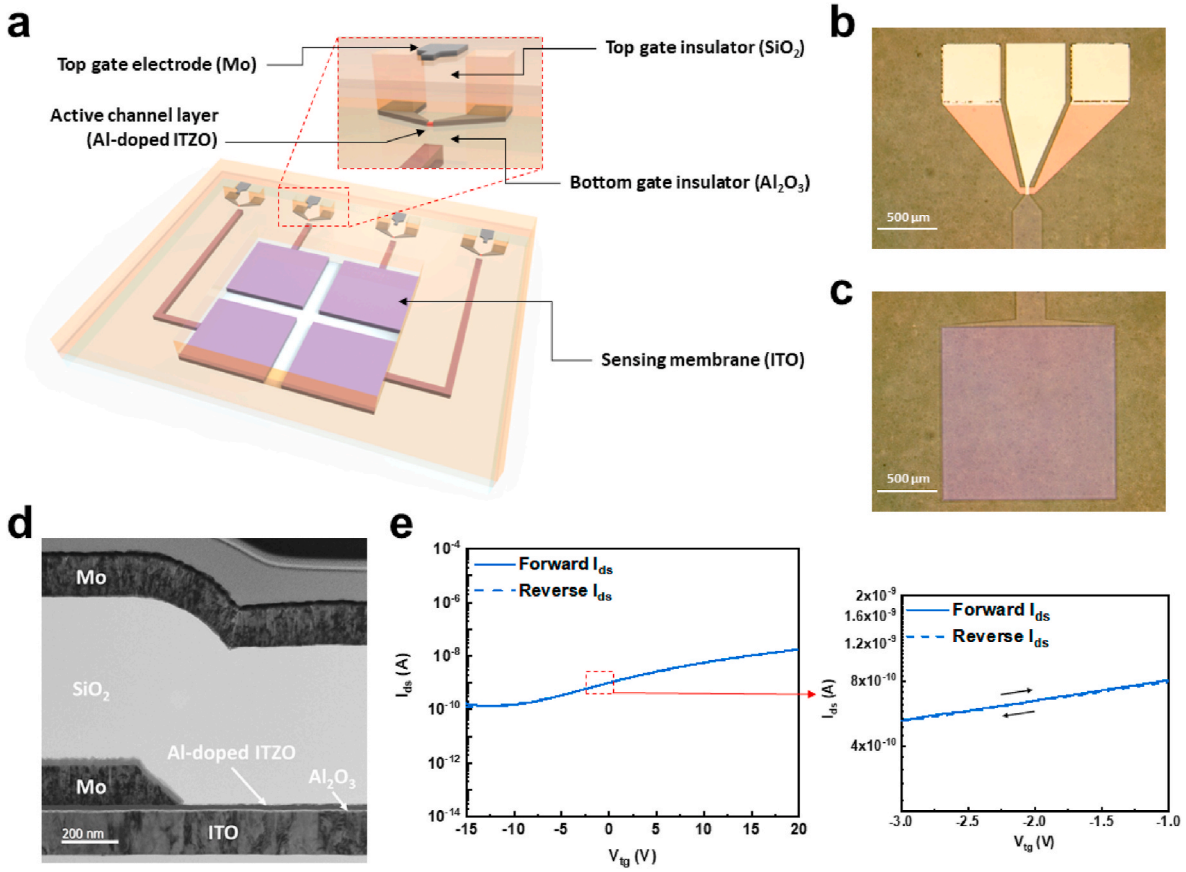


**Fig. 1.** Immunosensor based on a dual-gate oxide semiconductor thin-film transistor. (a) schematic illustration of the immunosensor structure. Top-view optical microscope images of the (b) thin-film transistor and (c) sensing membrane components. (d) Side-view TEM image. (e) Transfer characteristics.

successful binding of APTES to the surface.

We analyzed the surface of antibody-coated glass by AFM analysis. AFM operates by detecting the van der Waals forces between the tip and the atoms on the sample surface, thereby scanning the sample's topography. Through this, antibody binding on the glass surface was confirmed. In contrast to glass solely coated with APTES, which exhibits a curvature range of -2.0 to 2.0 nm, glass with attached antibodies displays a curvature difference of -7.9 to 7.7 nm (Figs. S3c–d). This suggests a firm binding of the antibody to the surface, especially considering the 14.5 nm height of the IgG antibody (Tan et al., 2008).

In addition, antibody attachment was confirmed using direct ELISA. The coated primary antibody was specifically captured using a horseradish peroxidase (HRP) conjugated anti-IgG antibody (second antibody), and the optical density (OD) of the HRP reaction was determined at 450 nm. With an increase in the number of antibodies coated on the glass surface, the binding of the secondary antibody also escalates, leading to a higher OD value. The OD value was 0.23 at a primary antibody concentration of 0 μg/mL, however, the OD value reached 0.87 when the primary antibody concentration was 1000 μg/mL (Fig. S3f). It can be confirmed that as the quantity of primary antibodies increases, the glass surface becomes more coated. High-density antibodies attached to the surface create an environment that efficiently captures proteins or viruses. Especially, at a coating concentration of 1000 μg/mL, there is nearly no deviation value, suggesting the possibility of achieving uniform antibody coating.

### 3.3. Real-time target protein and virus detection

The dual-gate TFT-based multiplex immunosensor was designed to detect three viruses simultaneously and therefore incorporated four sensing membranes, *including three main sensors and one canceling sensor*. *The performance of the immunosensor was confirmed by sensing target proteins of each main sensor, influenza A* pH*1N1 HA protein, SARS-CoV-2 S1 protein, or RSV fusion protein. Following target proteins, sensing performance for cultured viruses of influenza A* pH*1N1, SARS-CoV-2, and RSV was confirmed.* As injection of buffer solution or non-target sample can affect the surface potential of the sensing membrane and change the $I_{ds}$ (J. Kim et al., 2022; Seo et al., 2020), the canceling sensor was used to detect the rate of $I_{ds}$ change as a result of buffer solution or non-target sample injection. The canceling sensor was applied to overcome the disadvantage that the level of noise also increases as the degree of amplification increases. As subtracting the $I_{ds}$ change rate of the canceling sensor significantly reduced the $I_{ds}$ change rate of the main sensors for non-target samples (Fig. S4), the normalized response was calculated by subtracting the $I_{ds}$ change rate of the canceling sensor from the $I_{ds}$ change of the main sensor 60 s after sample injection. This canceling sensor measured and suppressed the response caused by non-target elements as shown on Fig. S4 to reduce the possibility of false-positives and allow precise target detection. The immobilized antibody on sensing membrane bound the target viral proteins that caused the change of surface potential (J. Kim et al., 2022), and this electrical signal is transmitted to the sensors as a change in bottom gate bias of dual-gate TFTs and normalized current variation along with signal amplification. The dual-gate TFT-based multiplex immunosensor was used to measure real-time normalized current variation. The selectivity of the main sensors was determined based on normalized responses for a high-concentration (1 pg/mL) sample (Fig. 2a). Non-target proteins exhibited negligible normalized responses of less than 0.1 (Figs. S5a–f), whereas rapid, large changes in normalized current were seen after injection of the target proteins (Fig. 2b–d). All three main sensors exhibited noticeable reactivity within 60 s, the time interval required to measure and calculate the normalized response. The

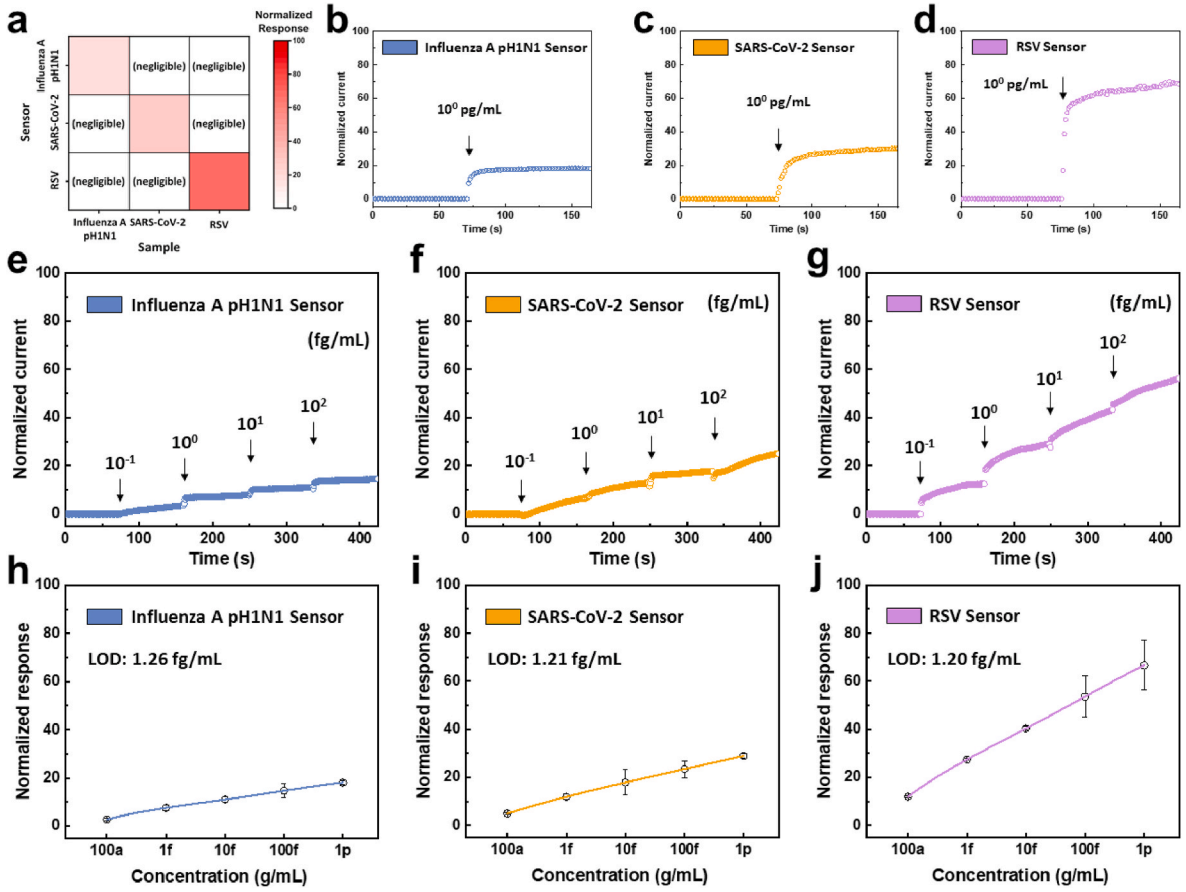


**Fig. 2.** (a) Selectivity cross-check by high-concentration sample detection. Normalized response variation by a high-concentration sample of (b) influenza A pH1N1 HA protein, (C) SARS-CoV-2 S1 protein, and (d) RSV fusion protein. Normalized response variation during real-time detection of (e) influenza A pH1N1 HA protein, (f) SARS-CoV-2 S1 protein, and (g) RSV fusion protein with increasing concentration. Calibration plots of normalized response 60 s after injection of (h) influenza A pH1N1 HA protein, (i) SARS-CoV-2 S1 protein, and (j) RSV fusion protein. The limit of detection (LOD) is indicated on the calibration plots.

influenza A pH1N1, SARS-CoV-2, and RSV sensors exhibited normalized responses of 18.1, 28.9, and 66.7, respectively. The sensitivity of the main sensors was determined by injecting four drops of the target protein sample with a wide concentration range (0.1–100 fg/mL), and the concentration range of the non-target proteins was same as that of target protein samples. The non-target proteins elicited negligible normalized responses of less than 0.1 (Fig. S5g–l), whereas the target protein samples induced significant real-time changes in the normalized currents (Fig. 2e–g). The calibration plots show normalized responses at each concentration, with LODs of the influenza A pH1N1, SARS-CoV-2, and RSV sensors of 1.26, 1.21, and 1.20 fg/mL, respectively (Fig. 2h–j). The types of FET and LODs for influenza A pH1N1, SARS-CoV-2, and RSV of previous FET-based immune-biosensors are summarized in Table S1. Our results confirmed that the main sensors in the immunosensor have outstanding selectivity and sensitivity for the target proteins.

Viruses targeted by the main sensors were bound on the sensing membrane via antibody–antigen reactions of specific viral proteins. The surface potential change was induced by charged proteins in the buffer solution with the screening of the area over the Debye length and transmitted to sensors as electrical signals (Stern et al., 2007), which changed the current in real-time with a high amplification factor. The selectivity and sensitivity of the dual-gate TFT-based multiplex immunosensor for the actual viruses were evaluated in real-time by measuring normalized current variation after injection of one drop of high-concentration ($10^3$ $TCID_{50}$/mL) samples of cultured influenza A pH1N1, SARS-CoV-2, and RSV (Fig. 3b–d). As shown in Fig. 3a, the main sensors exhibited high selectivity for the target viruses. Similar to the results for the target proteins, the injection of cultured viruses induced rapid changes in the normalized currents, whereas negligible normalized responses of less than 0.1 were seen for non-target viruses at the same concentration (Figs. S6a–f). Cultured influenza A pH1N1, SARS-CoV-2, and RSV induced high reactivity with normalized responses of 2.09, 3.37, and 5.85, respectively. Evaluation and quantification of sensitivity, by measuring normalized current variations with concentration gradient from $10^{-1}$ to $10^2$ $TCID_{50}$/mL of each virus sample individually (Fig. 3e–g), revealed rapid real-time changes in the normalized currents of the main sensors across a wide concentration range, with higher target virus concentrations inducing greater changes in normalized current. Non-target viruses, used as controls, induced negligible changes of less than 0.1 in the normalized response even at high concentrations (Fig. S6g–l). Influenza A pH1N1, SARS-CoV-2, and RSV sensors exhibited LODs of 2.02, 1.91, and 1.92 $TCID_{50}$/mL, respectively. These results confirmed that the immunosensor based on dual-gate oxide TFTs was promising device as diagnosis platform for target proteins and whole-cultured viruses with outstanding sensitivity, selectivity, short detection time within 60 s.

As the multiplexed immunosensor was designed to simultaneously detect influenza A pH1N1, SARS-CoV-2, and RSV, changes in the normalized responses to mixed cultured viruses with a wide concentration range ($10^{-1}$, $10^{\circ}$, $10^1$, and $10^2$ $TCID_{50}$/mL) in artificial saliva were also evaluated. Real-time normalized responses were reduced by only approximately 5% compared with those induced by single viruses in PBS solution (Fig. S7), confirming that the three viruses can be simultaneously detected in the saliva mixture.

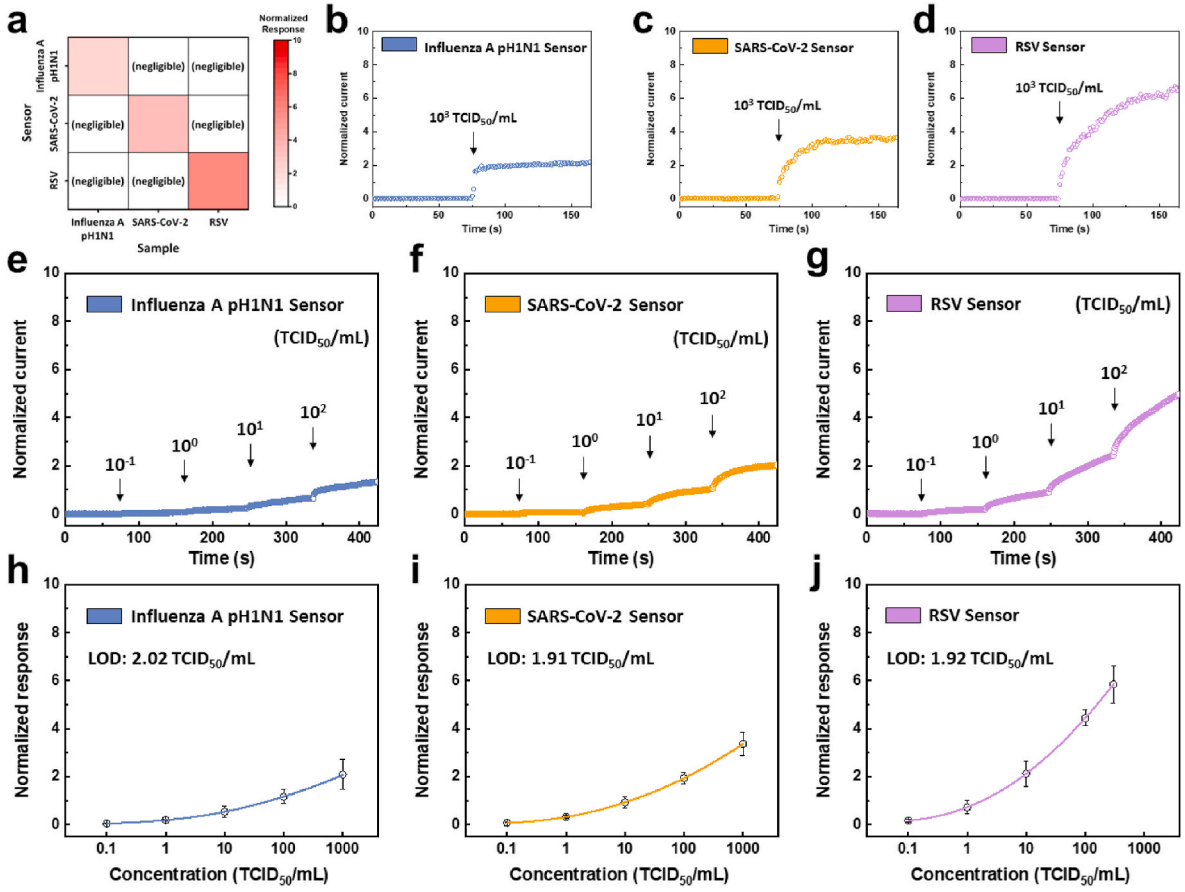


**Fig. 3.** (a) Selectivity cross-check by high-concentration sample detection. Normalized response variation by a high-concentration sample of (b) influenza A pH1N1, (C) SARS-CoV-2, and (d) RSV. Normalized response variation during real-time detection of (e) influenza A pH1N1, (f) SARS-CoV-2, and (g) RSV with increasing concentration. Calibration plots of normalized response 60 s after injection of (h) influenza A pH1N1, (i) SARS-CoV-2, and (j) RSV. The limit of detection (LOD) is indicated on the calibration plots.

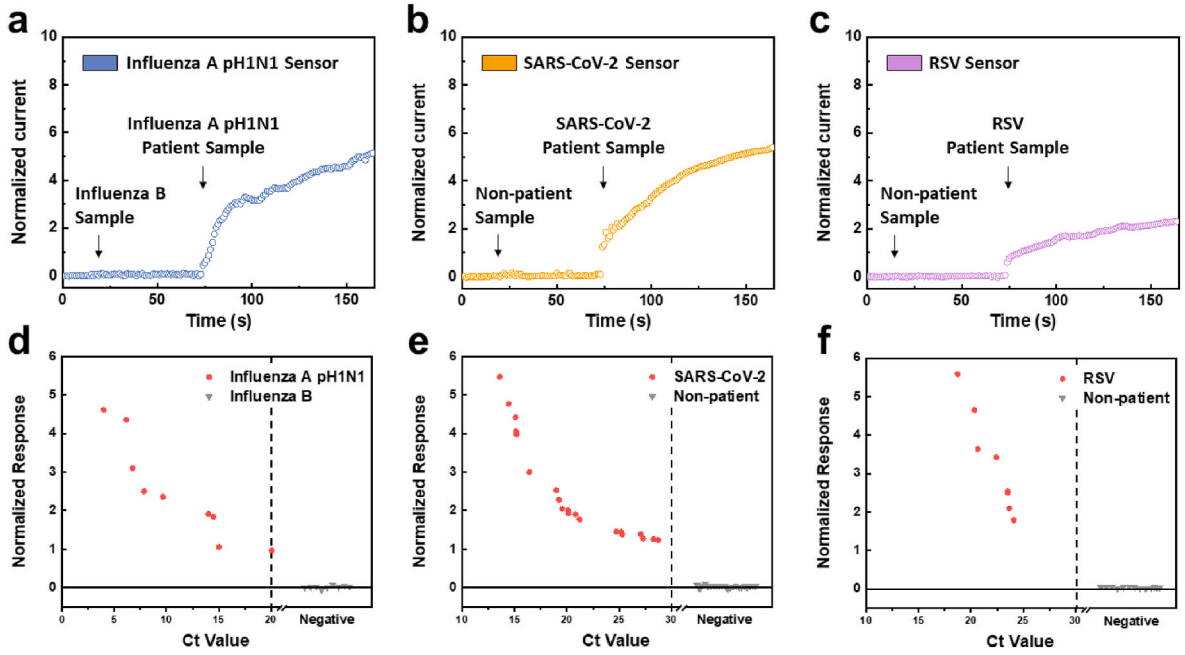


**Fig. 4.** Real-time detection of clinical samples from patients infected with (a) influenza A pH1N1 and influenza B. Variation of normalized current for clinical samples from patients infected with (b) SARS-CoV-2 and (c) RSV. (d) Normalized response of influenza A pH1N1 and influenza B as a function of cycle threshold (Ct) value. Normalized response of (e) SARS-CoV-2 and (f) RSV as a function of Ct value. Normalized response of (d) influenza A pH1N1, (e) SARS-CoV-2, and (f) RSV as a function of cycle threshold (Ct) value. Influenza B-infected and non-patient (uninfected) samples were used as a negative control.

### 3.4. Performance of the sensor on clinical samples

The real-world diagnostic ability of our multiplex immunosensor was evaluated using clinical samples obtained from the nasopharynx of patients infected with influenza A pH1N1, SARS-CoV-2, and RSV. Virus concentrations in clinical samples were considered cycle threshold (Ct) values, the number of cycles required to reach a certain detection threshold with PCR (Rabaan et al., 2021). A lower Ct value indicates a higher concentration of virus in the patient sample. To determine the selectivity and sensitivity for clinical samples of influenza A pH1N1, a drop of influenza B clinical sample was injected as a control, followed by a drop of influenza A pH1N1 clinical sample (Fig. 4a). Normalized responses measured 60 s after sample injection of influenza A pH1N1 and influenza B were plotted as a function of Ct values (Fig. 4d). For SARS-CoV-2 and RSV, a drop of non-patient (uninfected control) sample was first injected, followed by a drop of a clinical sample (Fig. 4b and c). Real-time normalized current variations were measured, and the normalized response 60 s after sample injection was plotted as a function of Ct values (Fig. 4e and f). Clinical samples of influenza A pH1N1, SARS-CoV-2, and RSV induced rapid and notable reactivity, whereas negative (uninfected control) samples induced negligible changes in normalized current. Correlations between normalized response and Ct values revealed a greater normalized response for smaller Ct values, indicating higher viral concentrations in clinical samples. All diagnosis results conducted through a blind review were consistent with the qRT-PCR results, and neither false positives nor false negatives have been confirmed.

The multiplex immunosensor can, therefore, accurately and rapidly identify target viruses in real-world clinical samples without requiring any pretreatment or additional amplification devices.

## 4. Conclusion

We developed a rapid and sensitive multiplex immunosensor based on dual-gate oxide semiconductor TFTs (dual-gate TFT-based multiplex immunosensor) to diagnose a tripledemic—a simultaneous infection with three prominent respiratory viruses (influenza A pH1N1, SARS-CoV-2, and RSV) with similar symptoms. The dual-gate TFT structure was optimized, and sensor performance was confirmed. The sensitivity of the immunosensor was not only improved by operating in the subthreshold regime, but also enhanced by the capacitive coupling through GI adjusting. The dual-gate oxide TFT showed outstanding capacitive coupling ratio of 120.17 $\pm$ 3.17 V/V with optimized GI. This sensor could detect both the target protein and whole virus within a short time ($\leq$60 s) through antibody-antigen interaction and signal amplification. The variable heavy chain (VH) and variable light chain (VL) domains of the antibodies used on each immunosensor are capable of recognizing and capturing specific proteins. Therefore, they were able to distinguish among the three types of viruses in the saliva mixture. Furthermore, the sensor was able to identify viruses in a total 60 clinical samples, including 39 patients infected with influenza A pH1N1, SARS-CoV-2 and RSV, and when compared with qRT-PCR results, it was able to detect with high accuracy without false positives or false negatives. The sensor can, therefore, be used for rapid and sensitive diagnosis of patients with similar symptoms. This can lead to efficient treatment is possible by prescribing appropriate medications and treatment methods, and time-consuming medical overload due to triple disease can be reduced. Our multiplexed immunosensor is a valuable diagnostic platform capable of responding to current and future pandemic viruses. This immunosensor exhibits exceptional detection capabilities, diagnosing various diseases by detecting disease-related biomarkers (such as proteins and exosomes) in body fluids. This suggests the potential for utilization as an in vitro diagnostic (IVD) platform in the field of liquid biopsy.

## CRediT authorship contribution statement

**Sehun Jeong:** Conceptualization, Methodology, Result analysis, Visualization, Writing, Validation. **Seong Uk Son:** Methodology, Result analysis, Visualization, Data curation, Writing, Validation. **Jingyu Kim:** Conceptualization, Result analysis. **Seong-In Cho:** Data curation, Result analysis. **Taejoon Kang:** Methodology, Resources. **Sunjoo Kim:** Methodology, Resources. **Eun-Kyung Lim:** Supervision, Conceptualization, Funding acquisition, Writing – review & editing. **Sang-Hee Ko Park:** Supervision, Funding acquisition, Writing – review & editing.

## Declaration of competing interest

The authors declare that they have no known competing financial interests or personal relationships that could have appeared to influence the work reported in this paper.

## Data availability

No data was used for the research described in the article.

## Acknowledgements

This work was supported by the Ministry of Trade, Industry & Energy (Korea) [grant number 20016319]; the National Research Foundation grants funded by the Korean Government (Ministry of Science and ICT, MSIT) [grant number NRF-2021M3E5E3080379, NRF-2022R1C1C1008815, and NRF-2022M3E5F4078558]; the Technology Development Program for Biological Hazards Management in Indoor Air through the Korea Environmental Industry & Technology Institute funded by the Korean Government [grant number 2021003370003]; and the Korea Research Institute of Bioscience and Biotechnology Research Initiative Program [grant number KGM5472322].

## Appendix A. Supplementary data

Supplementary data to this article can be found online at https://doi.org/10.1016/j.bios.2023.115700.

## References

Afroj, S., Britnell, L., Hasan, T., Andreeva, D.V., Novoselov, K.S., Karim, N., 2021. Adv. Funct. Mater. 31, 2107407.
Ahn, J.H., Choi, B., Choi, S.J., 2020. J. Appl. Phys. 128.
Baek, G., Kanicki, J., 2012. J. Soc. Inf. Disp. 20, 237–244.
Baek, S., Matsui, H., Mano, T., Park, J.A., Jo, Y., Lee, Y., Tokito, S., Kwon, J., Jung, S., 2023. Biosens. Bioelectron. 222, 114958.
Baker, R.E., Mahmud, A.S., Miller, I.F., Rajeev, M., Rasambainarivo, F., Rice, B.L., Takahashi, S., Tatem, A.J., Wagner, C.E., Wang, L.F., Wesolowski, A., Metcalf, C.J.E., 2022. Nat. Rev. Microbiol. 20, 193–205.
Baldacchini, C., Montanarella, A.F., Francioso, L., Signore, M.A., Cannistraro, S., Bizzarri, A.R., 2020. Sensors 20, 6364.
Barron, A.R., 1996. Adv. Mater. Opt. Electron. 6, 101–114.
Chandra Barman, S., Sharifuzzaman, M., Zahed, M.A., Park, C., Yoon, S.H., Zhang, S., Kim, H., Yoon, H., Park, J.Y., 2021. Biosens. Bioelectron. 186, 113287.
Chen, G., Shen, S., Tat, T., Zhao, X., Zhou, Y., Fang, Y., Chen, J., 2022. View 3, 1–9.
Chen, J., Pu, H., Hersam, M.C., Westerhoff, P., 2022. Adv. Mater. 34, 1–14.
Chen, R., Zhou, W., Zhang, M., Wong, M., Kwok, H.S., 2013. Thin Solid Films 548, 572–575.
Cho, S.I., Ko, J.B., Lee, S.H., Kim, J., Park, S.H.K., 2022. J. Alloys Compd. 893, 162308.
Choi, W.H., Jeon, W., Park, J.S., 2020. J. Mater. Chem. C 8, 13342–13348.
Das, A., Ko, D.H., Chen, C.H., Chang, L.B., Lai, C.S., Chu, F.C., Chow, L., Lin, R.M., 2014. Sensor. Actuator. B Chem. 205, 199–205.
Deng, Y., Liu, L., Li, J., Gao, L., 2022. Biosensors 12.
Dingemans, G., van Helvoirt, C.A.A., Pierreux, D., Keuning, W., Kessels, W.M.M., 2012. J. Electrochem. Soc. 159, H277–H285.
Fathi-Hafshejani, P., Azam, N., Wang, L., Kuroda, M.A., Hamilton, M.C., Hasim, S., Mahjouri-Samani, M., 2021. ACS Nano 15, 11461–11469.
Fuh, C.S., Liu, P.T., Huang, W.H., Sze, S.M., 2014. IEEE Electron. Device Lett. 35, 1103–1105.
Gao, X.P.A., Zheng, G., Lieber, C.M., 2010. Nano Lett. 10, 547–552.

Hwang, M.T., Heiranian, M., Kim, Y., You, S., Leem, J., Taqieddin, A., Faramarzi, V., Jing, Y., Park, I., van der Zande, A.M., Nam, S., Aluru, N.R., Bashir, R., 2020. Nat. Commun. 11.
Jang, Y.W., Kang, J., Jo, J.W., Kim, Y.H., Kim, J., Park, S.K., 2021. Sensor. Actuator. B Chem. 342, 130058.
Ji, S., Jang, J., Hwang, J.C., Lee, Y., Lee, J.H., Park, J.U., 2020. Adv. Mater. Technol. 5, 1–9.
Jung, H., Kim, W.H., Oh, I.K., Lee, C.W., Lansalot-Matras, C., Lee, S.J., Myoung, J.M., Lee, H.B.R., Kim, H., 2016. J. Mater. Sci. 51, 5082–5091.
Kajale, S.N., Yadav, S., Cai, Y., Joy, B., Sarkar, D., 2021. iScience 24, 103513.
Kamiya, T., Nomura, K., Hosono, H., 2010. Sci. Technol. Adv. Mater. 11.
Kang, B., Lee, Y., Lim, J., Yong, D., Ki Choi, Y., Woo Yoon, S., Seo, S., Jang, S., Uk Son, S., Kang, T., Jung, J., Lee, K.S., Kim, M.H., Lim, E.K., 2022. Chem. Eng. J. 442, 136143.
Kang, M.J., Yoon, Y., Je, B.-K., Kim, Y.K., Seo, W.H., 2023. Displays 11, 48.
Kekatos, M., 2022. Is the US Facing a Potential "Tripledemic" of Flu, RSV and COVID-19? ABC News. https://abcnews.go.com/Health/us-facing-potential-tripledemic-flu-rsv-covid-19/story?id=91997909. (Accessed 26 October 2022).
Kim, E., Lim, E.K., Park, G., Park, C., Lim, J.W., Lee, H., Na, W., Yeom, M., Kim, J., Song, D., Haam, S., 2021. Adv. Mater. 33, 1–32.
Kim, J., Jeong, S., Sarawut, S., Kim, H., Son, S.U., Lee, S., Rabbani, G., Kwon, H., Lim, E. K., Ahn, S.N., Park, S.H.K., 2022. Lab Chip 22, 899–907.
Kim, J.B., Fuentes-Hernandez, C., Potscavage, W.J., Zhang, X.H., Kippelen, B., 2009. Appl. Phys. Lett. 94, 9–12.
Kim, T.Y., Bae, G.E., Kim, J.Y., Kang, M., Jang, J.H., Huh, H.J., Chung, D.R., Lee, N.Y., 2022. PLoS One 17, 1–10.
Knopfmacher, O., Tarasov, A., Fu, W., Wipf, M., Niesen, B., Calame, M., Schönenberger, C., 2010. Nano Lett. 10, 2268–2274.
Ko, J.B., Lee, S.H., Park, K.W., Park, S.H.K., 2019. RSC Adv. 9, 36293–36300.
Kwon, S.S., Kim, D., Yun, M., Son, J.G., Lee, S.H., 2021. Biosens. Bioelectron. 192, 113519.
Lee, J., Kim, M.J., Yang, H., Kim, S., Yeom, S., Ryu, G., Shin, Y., Sul, O., Jeong, J.K., Lee, S.B., 2021. IEEE Sensor. J. 21, 178–184.
Li, Yan, Wang, J., Wang, C., Yang, Q., Xu, Y., Xu, J., Li, Yi, Yu, X., Zhu, H., Liu, J., 2020. Int. J. Infect. Dis. 96, 266–269.
Liu, X., Huang, L., Qian, K., 2021. Adv. NanoBiomed Res. 1, 2000104.
Ma, P., Du, L., Wang, Y., Jiang, R., Xin, Q., Li, Y., Song, A., 2018. Appl. Phys. Lett. 112.
Manigrasso, J., Chillón, I., Genna, V., Vidossich, P., Somarowthu, S., Pyle, A.M., De Vivo, M., Marcia, M., 2022. Nat. Commun. 13, 41467.
Martins, E. de F., Pinotti, L.F., Silva, C. de C.C., Rocha, A.R., 2021. Chemosensors 9.
Masurkar, N., Varma, S., Mohana Reddy Arava, L., 2020. Electrochemistry (Tokyo, Jpn.) 1, 260–277.
Merced-Morales, A., Daly, P., Anwar, I., Elal, A., Ajayi, N., Annan, E., Budd, A., Barnes, J., Colon, A., Cummings, C.N., Iuliano, A.D., Dasilva, J., Dempster, N., Garg, S., Gubareva, L., Hawkins, D., Howa, A., Huang, S., Kirby, M., Kniss, K., Kondor, R., Liddell, J., Moon, S., Nguyen, H.T., O'halloran, A., Smith, C., Stark, T., Tastad, K., Ujamaa, D., Wentworth, D.E., Fry, A.M., Dugan, V.G., Brammer, L., 2022. Morb. Mortal. Wkly. Rep. 71, 913–919.
Moon, J., Kwon, H.J., Yong, D., Lee, I.C., Kim, H., Kang, H., Lim, E.K., Lee, K.S., Jung, J., Park, H.G., Kang, T., 2020. ACS Sens. 5, 4017–4026.
Ovanesyan, R.A., Filatova, E.A., Elliott, S.D., Hausmann, D.M., Smith, D.C., Agarwal, S., 2019. J. Vac. Sci. Technol. A Vacuum, Surfaces, Film 37.
Park, H., Baek, S., Sen, A., Jung, B., Shim, J., Park, Y.C., Lee, L.P., Kim, Y.J., Kim, S., 2022. ACS Nano 16, 1826–1835.
Park, J.S., Sheng, J., Han, J.H., Choi, W.H., Park, J., 2017. ACS Appl. Mater. Interfaces 9, 42928–42934.
Park, S.J., Kwon, O.S., Lee, S.H., Song, H.S., Park, T.H., Jang, J., 2012. Nano Lett. 12, 5082–5090.
Piccinini, E., Fenoy, G.E., Cantillo, A.L., Allegretto, J.A., Scotto, J., Piccinini, J.M., Marmisollé, W.A., Azzaroni, O., 2022. Adv. Mater. Interfac. 9, 1–11.
Poghossian, A., Jablonski, M., Molinnus, D., Wege, C., Schöning, M.J., 2020. Front. Plant Sci. 11, 1–14.
Rabaan, A.A., Tirupathi, R., Sule, A.A., Aldali, J., Mutair, A. Al, Alhumaid, S., Muzaheed, Gupta, N., Koritala, T., Adhikari, R., Bilal, M., Dhawan, M., Tiwari, R., Mitra, S., Emran, T. Bin, Dhama, K., 2021. Diagnostics 11.
Ranjan, P., Thomas, V., Kumar, P., 2021. J. Mater. Chem. B 9, 4608–4619.
Ravina Dalal, A., Mohan, H., Prasad, M., Pundir, C.S., 2020. Biosci. Rep. 40, 1–18.
Ruest, A., Michaud, S., Deslandes, S., Frost, E.H., 2003. J. Clin. Microbiol. 41, 3487–3493.
Sadighbayan, D., Hasanzadeh, M., Ghafar-Zadeh, E., 2020. TrAC, Trends Anal. Chem. 133, 116067.
Seo, G., Lee, G., Kim, M.J., Baek, S.H., Choi, M., Ku, K.B., Lee, C.S., Jun, S., Park, D., Kim, H.G., Kim, S.J., Lee, J.O., Kim, B.T., Park, E.C., Kim, S. Il, 2020. ACS Nano 14, 5135–5142.
Shahdeo, D., Chauhan, N., Majumdar, A., Ghosh, A., Gandhi, S., 2022. ACS Appl. Bio Mater. 5, 3563–3572.
Shukla, S.K., Patra, S., Das, T.R., Kumar, D., Mishra, A., Tiwari, A., 2022. View 3, 1–18.
Son, S.U., Jang, S., Lim, J., Seo, S.B., Kang, T., Jung, J., Oh, S.Y., Yoon, S.W., Yong, D., Lee, J., Lim, E.K., 2023. ACS Appl. Mater. Interfaces 15, 7759–7766.
Son, S.U., Seo, S.B., Jang, S., Choi, J., Lim, J. woo, Lee, D.K., Kim, H., Seo, S., Kang, T., Jung, J., Lim, E.K., 2019. Sensor. Actuator. B Chem. 291, 257–265.
Stern, E., Wagner, R., Sigworth, F.J., Breaker, R., Fahmy, T.M., Reed, M.A., 2007. Nano Lett. 7, 3405–3409.
Tan, Y.H., Liu, M., Nolting, B., Go, J.G., Gervay-hague, J., Liu, G., 2008. ACS Nano 2, 2374–2384.
Tang, Z., Kong, N., Zhang, X., Liu, Y., Hu, P., Mou, S., Liljeström, P., Shi, J., Tan, W., Kim, J.S., Cao, Y., Langer, R., Leong, K.W., Farokhzad, O.C., Tao, W., 2020. Nat. Rev. Mater. 5, 847–860.
Tlili, C., Myung, N.V., Shetty, V., Mulchandani, A., 2011. Biosens. Bioelectron. 26, 4382–4386.
Todd, A.K., Costa, A.M., Waller, G., Daley, A.J., Barr, I.G., Deng, Y.M., 2021. J. Virol. Methods 294.
Wang, B., Zhao, C., Wang, Z., Yang, K.A., Cheng, X., Liu, W., Yu, W., Lin, S., Zhao, Y., Cheung, K.M., Lin, H., Hojaiji, H., Weiss, P.S., Stojanović, M.N., Tomiyama, A.J., Andrews, A.M., Emaminejad, S., 2022a. Sci. Adv. 8, 1–16.
Wang, Y., Li, B., Tian, T., Liu, Y., Zhang, J., Qian, K., 2022b. TrAC, Trends Anal. Chem. 149.
Yahya, I., Hassan, M.A., Maidin, N.N.M., Mohamed, M.A., 2022. Sensors 22, 8212.
Ye, Z., Yuan, Y., Xu, H., Liu, Y., Luo, J., Wong, M., 2017. IEEE Trans. Electron. Dev. 64, 438–446.
Zamzami, M.A., Rabbani, G., Ahmad, A., Basalah, A.A., Al-Sabban, W.H., Nate Ahn, S., Choudhry, H., 2022. Bioelectrochemistry 143.
Zhang, S., Wan, Z., Pavlou, G., Zhong, A.X., Xu, L., Kamm, R.D., 2022. Adv. Funct. Mater. 32.
Zhao, C., Cheung, K.M., Huang, I.W., Yang, H., Nakatsuka, N., Liu, W., Cao, Y., Man, T., Weiss, P.S., Monbouquette, H.G., Andrews, A.M., 2021. Sci. Adv. 7, 25–27.
Zheng, Y., Song, X., Fredj, Z., Bian, S., Sawan, M., 2023. Anal. Chim. Acta 1244, 340860.